Int J Earth Sci (Geol Rundsch) (2017) 106:1057–1073
DOI 10.1007/s00531-016-1353-9

ORIGINAL PAPER

Invisible gold distribution on pyrite and ore-forming fluid process of the Huangshan orogenic-type gold deposit of Zhejiang, SE China: implications from mineralogy, trace elements, impurity and fluid inclusion studies

Vijay Anand Sundarrajan[1,2] · Zilong Li[1] · Yizhou Hu[1] · Xuheng Fu[1] · Yuhuo Zhu[3]

Received: 7 September 2015 / Accepted: 5 June 2016 / Published online: 18 July 2016
© Springer-Verlag Berlin Heidelberg 2016

Abstract The Huangshan orogenic-type gold deposit in Zhejiang of SE China occurred in quartz–pyrite veins. It is hosted by phyllonite that underwent greenschist-facies metamorphism along a large Jiangshan–Shaoxing tectonic belt with a NE–SW direction. Trace elemental characteristics, ore-forming process and invisible gold on different forms of pyrite and quartz are studied. The Au associated pyrite can be classified into two categories; recrystallized pyrite and euhedral pyrite. The precipitation of invisible Au on pyrite is mainly derived by Co and Ni with $AuHS_2^-$ complex in the mineralizing fluids in different events. The XPS results revealed that valence states of Au^{3+} replaced $2Fe^{2+}$ in the pyrite and Au^0 replaced Si^{4+} in the quartz structure. The electron paramagnetic resonance and trace elemental results suggested that the element pairs of Ge–Li–Al in quartz and Mn–Co–Ni in pyrite have distinct impurities as identified. A fluid inclusion study showed that the auriferous quartz is characterized by low-saline and CO_2-rich fluids. Coexistence of the type I–type III inclusions and same range of homogenization temperature with different mode are evidences of immiscible fluid process. The temperature–pressure values of ca. 250 °C/1250 bar and ca. 220 °C/780 bar for gold precipitation have been calculated by intersection of coexisting fluids during the entrapment. The Huangshan orogenic-type gold deposit may be associated with the Wuyi–Yunkai orogeny during the early Paleozoic, including an upper–mid greenschist-facies metamorphism (450–420 Ma). All the features suggest that the Huangshan gold deposit is probably a product linking with the early Paleozoic orogeny in South China.

Keywords Early Paleozoic orogeny · Ductile shear zone · Huangshan · Greenschist-facies · Fluid inclusion · Quartz–pyrite vein

Introduction

Quartz and pyrite occurred in varied gold-mineralized environments in high- to low-grade metamorphic terrenes (Gotze 2009; Thomas et al. 2011; Deditius et al. 2014, and references therein). In different zones, quartz and pyrite are characterized by different forms, as a consequence of crystallization and origin (Large et al. 2009; Cook et al. 2009; Sung et al. 2009). In recent decades, studies on quartz and pyrite in different gold deposits by electron probe microanalyzer (EPMA) and LA-ICP-MS methods revealed high concentration of invisible gold distribution and trace element abundances (Ciobanu et al. 2012; Palenik et al. 2004; Reich et al. 2005, 2006; Cook et al. 2009; Su et al. 2012). The size and chemical state of Au may incorporate on the quartz and pyrite lattice through the substitution in Si^{4+} and $2Fe^{2+}$ structures, respectively (Nuttall and Weil 1981a, b, c; Weil 1984, 1993; Wilson et al. 1986; Fowler et al. 1987; Ikeya 1993; Mikhlin and Romanchenko (2007)).

The type and origin of gold deposits are well documented in the aspects of fluid inclusion, trace elemental and isotopic geochemistry (Groves et al. 1998, 2003; Goldfarb et al. 2001, 2005; Kerrich et al. 2000; Zhang

✉ Zilong Li
zilongli@zju.edu.cn

[1] School of Earth Sciences, Zhejiang University, 38 Zheda Road, Hangzhou 310027, People's Republic of China

[2] Department of Earth Sciences, Eritrea Institute of Technology, Asmara 12676, Eritrea

[3] Zhejiang Xinsheng Gold Limited Company, Zhuji 311809, People's Republic of China

et al. 2004; Chen et al. 2012; Helmy and Zoheir 2015). The orogenic-type gold deposit is usually associated with upper–mid greenschist-facies metamorphism at convergent margins (Goldfarb et al. 2001; Groves et al. 2003). (1) The occurrences of the ore bodies are mainly controlled by its lithology and shearing events; (2) the ore mineralization is coeval, particularly occured at convergent margins; (3) the mineralization depth ranges are from <20 kms; and (4) the composition of ore fluid is H_2O with variable amount of carbonic-rich phases, generated from metamorphic dehydration process (Chen 2006, 2010; Goldfarb et al. 1998, 2001; Groves et al. 2003).

Numerous gold deposits, occurred along the Jiangshan–Shaoxing tectonic belt of SE China, have been identified during the period from the Proterozoic to Mesozoic (Chen and Xu 1996; Chen and Jahn 1997; Pirajno et al. 1997; Pirajno and Bagas 2002).

The Huangshan gold deposit is a typical one in Zhejiang Province, SE China. Its mineralization may be principally controlled by its structures, host rock geochemistry, metamorphic and hydrothermal processes (Chen and Xu 1996; Pirajno et al. 1997; Ni et al. 2015). The gold deposit occurs in a ductile shear zone with a NE–SW direction and was spatially associated with phyllonite and quartz–sulfide veins, respectively.

Ore deposits in the Zhejiang Province of SE China along the Jiang-Shao tectonic belt are poorly constrained, particularly for the Huangshan deposit, for which the ore-forming process, genesis and tectonic settings are poorly constrained. In this paper, the following studies are carried out: (1) trace element abundances in different forms of pyrite characterized by EPMA, (2) types and concentration of impurities in pyrite and quartz by EPR (electron paramagnetic resonance) spectroscopy, (3) types, composition and *P*–*T* conditions of ore fluids in auriferous quartz by fluid inclusion study and (4) whether high concentrations of invisible gold, size and chemical state of Au in quartz and pyrite are another significant contribution by X-ray photoelectron spectroscopic (XPS) study. They can provide better evidences to constrain the precipitation mechanism of gold, associated impurities in gold-mineralized zone, and nature and evolution of the ore-forming fluids, and finally, genesis of the Huangshan gold deposit will be discussed.

Geological setting of the Huangshan gold deposit

The South China Block (SCB) is composed of two major Precambrian continental blocks called the Yangtze Block and the Cathaysia Block divided by the Jiangshan–Shaoxing tectonic belt (as a Neoproterozoic suture zone between Yangtze and Cathaysia blocks) (Ren 1990; Li et al. 2007, 2009, 2010a). The Chencai–Suichang Uplift (CSU) in Zhejiang is an uplifted crustal block, in which the Proterozoic basement is exposed as tectonic windows in the overlying Mesozoic volcanic strata. Several Paleozoic and Mesozoic gold and polymetallic deposits are hosted by the high-grade metamorphosed basements in South China. Ore deposits of the CSU are parts of large and complex mineralizing systems, and each deposit is linked to the respective tectonic-magmatic event. Basement rocks are exposed in a series of tectonic windows, produced by tectonic uplift, and consist of upper amphibolite- to greenschist-facies rocks formed during the Paleozoic (Zhong et al. 1996).

The Huangshan orogenic gold deposit is located in the NE Shaoxing–Longquan Precambrian uplift in the central part of Zhejiang between the Jiangnan tectonic belt and Cathaysia block (Fig. 1a, b). The ore bodies occur on the NE–SW direction along the southern edge of the Jiangnan tectonic belt (Chen and Xu 1996; Chen and Jahn 1997; Pirajno et al. 1997; Ni et al. 2015) (Fig. 1c) with host rocks of the Chencai Group as the Proterozoic basement, which suffered upper greenschist- to amphibolite-facies metamorphism during the early Paleozoic. The Chencai–Suichang complex may be regarded as a part of a zone containing slices of oceanic crust, which cropped out sporadically between Shaoxing and Zhuji areas; and it represented as a suture resulting from collision and accretion defined by the NE–SW trending of the Jiangshan–Shaoxing tectonic belt (Chen and Xu 1996; Pirajno et al. 2009).

The deposit is primarily controlled by its lithology, alteration and deformation process that occurred in phyllonite and amphibolitic gneiss. The length of the ore body is about 500 m on the surface, and extends to the depth of about 200 m. The width of the ore zone ranges from 0.2 to 9 m with an average of 3 m. The average ore grade is 10.56 g/ton gold. The lenses of 0.5–1 m length are located along the NE strike of the ore zone dipping in the same direction. It occurs in cleavage planes parallel to the main fabric of the shear zone. Some of quartz–pyrite veins are strongly sheared, and in other cases, the vein is weakly sheared and massive, suggesting that at least three stages of vein emplacement occurred during the periods of pre-shearing, shearing and post-shearing events. The sample of quartz and pyrite was collected from shear stage for various experiments.

Sample description and analytical methods

Sample description

The samples of auriferous quartz and pyrite were collected in different parts of the phyllonite belt (Fig. 2). The

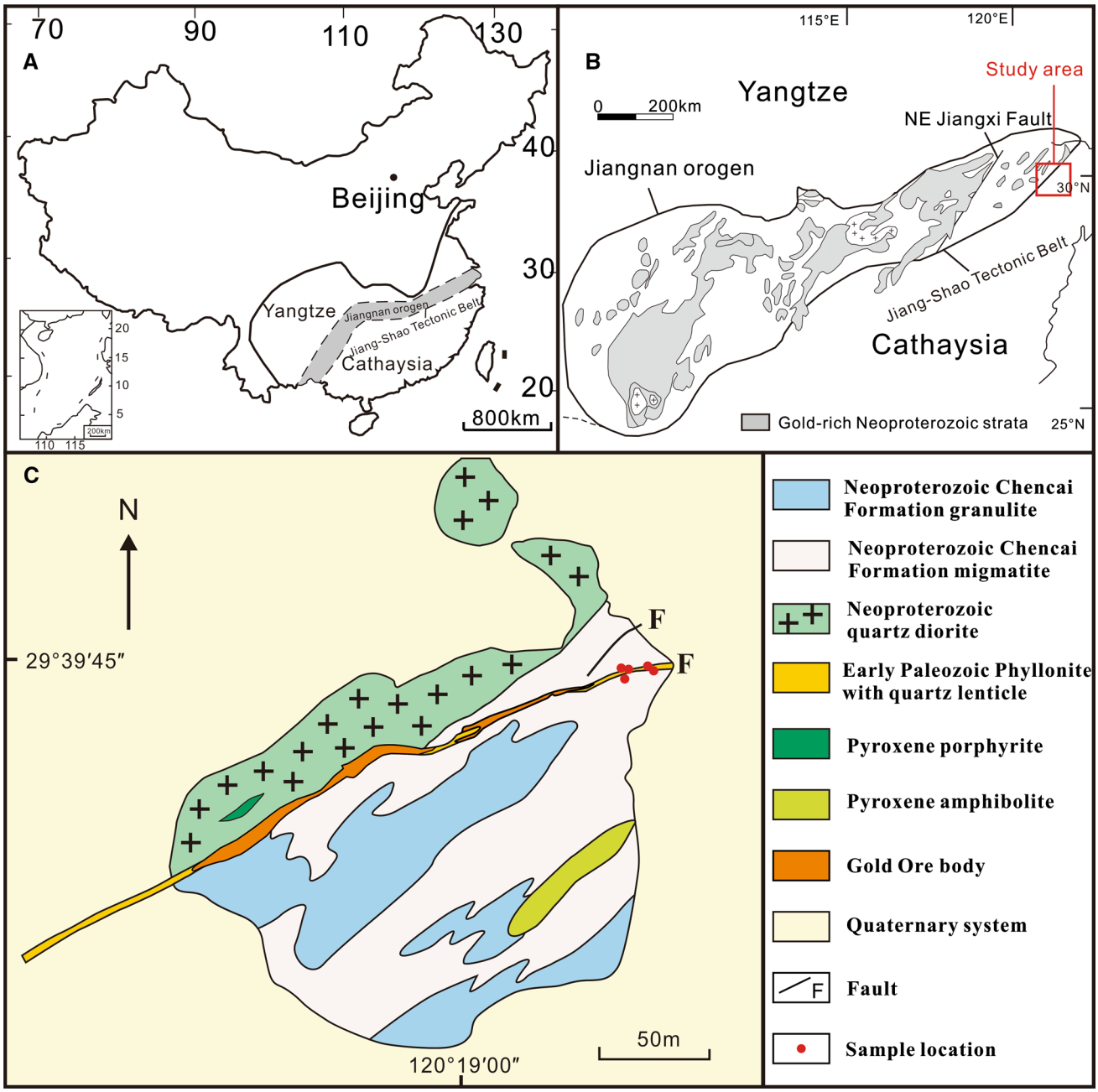

Fig. 1 **A** Location map of Huangshan in China (modified after Zhao et al. 2013); **B** location of Huangshan gold deposit along the Jiang-Shao tectonic belt (modified after Zhu et al. 2009; Ni et al. 2015); **C** geological map of Huangshan gold deposit in Zhejiang Province, SE China (modified after Zhu et al. 2009)

mineralization in the phyllonite belt occurs as irregular veins or cataclastic and mylonitic breccia. The alteration products in quartz–sulfide veins consist of quartz, chlorite, sericite and pyrite. The paragenetic sequences of silicate and ore minerals are classified and listed in Fig. 3.

Thirty ore samples were collected from different sites of underground horizons and studied for detailed ore petrography. The main ore minerals of pyrite, chalcopyrite, sphalerite and galena have been classified in decreasing order of abundance. The representative ore samples (13HS18, 13HS07, 13HS04) of auriferous quartz–pyrite have been selected for EPMA and XPS analyses.

EPMA

Trace elements are studied in pyrite grains using the EPMA in the Key Laboratory of the Secondary Institute of Oceanography, State Oceanic Administration in Hangzhou, P. R.

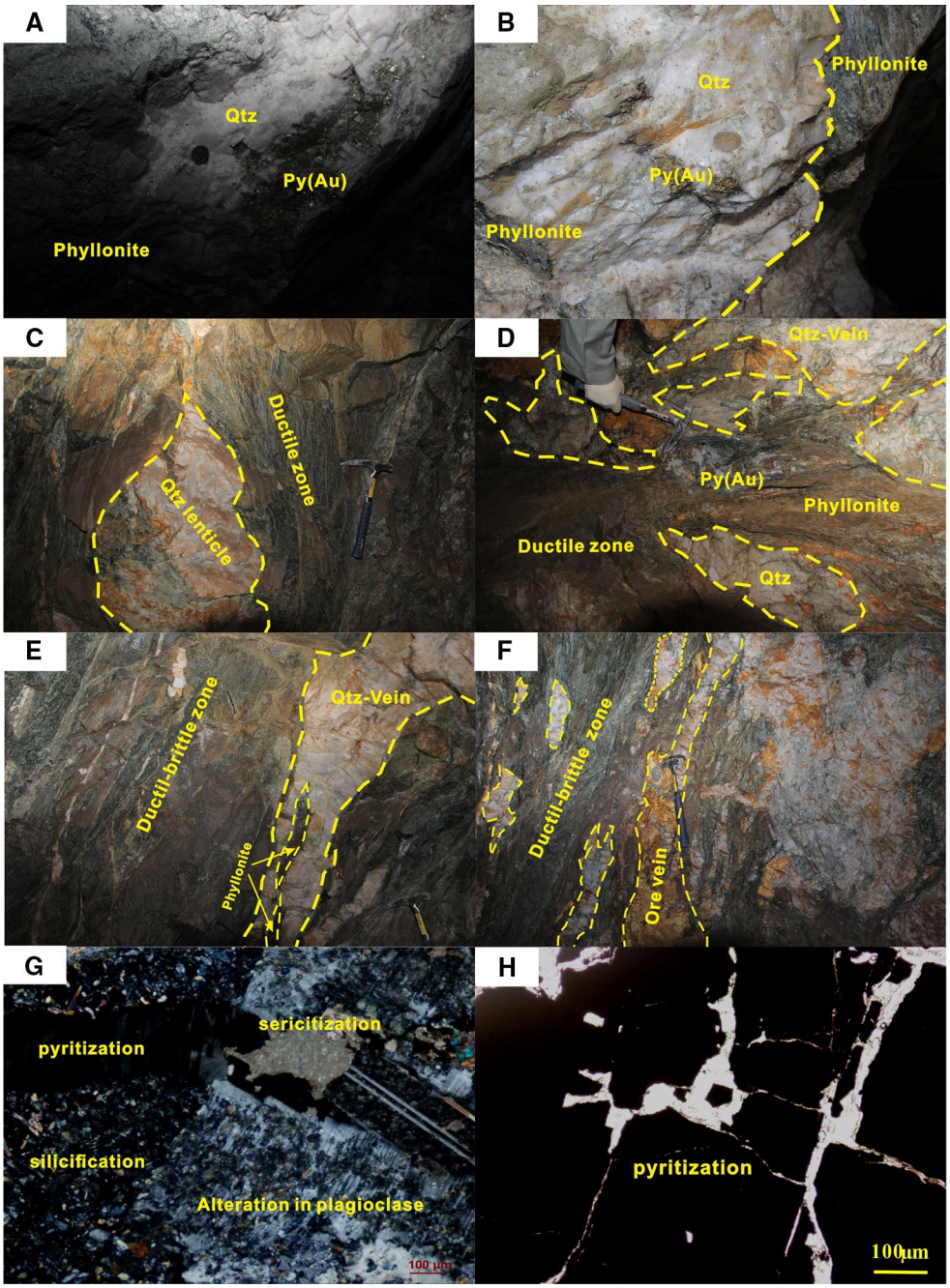

Fig. 2 Photographs of representative samples from the Huangshan orogenic-type gold deposit. **A**, **B** Quartz and pyrite (Au) veins in different sites of the phyllonite belt; **C**, **D** auriferous quartz lenticles and pyrite (Au) in ductile shear zone; **E**, **F** crenulation cleavage in quartz and phyllonite enclave observed in the ductile–brittle zone; and **G**, **H** alterated minerals include quartz, muscovite, plagioclase and pyrite. Abbreviations: Qtz, quartz; Py, pyrite

China. The analytical conditions for instrument were 20 kV accelerating voltage and 100 nA beam current. The count times for Fe and S were 20 s and for other elements were 80 s. The standards of the Fe-S (FeS_2), As_3 (As), Au (Au^0), Co (Co^0), Ni (Ni^0), Bi (Bi_2S_3), Te (Te^0) and Cu ($CuFeS_2$) were used for analyses.

XPS

The elements of Au ($4f_{7/2}$), Co ($2p_{3/2}$), Bi (4f) and Ge ($3d_{5/2}$) were standardized before analyses. The analytical penetration depth is 0.5–10 nm, and width is between 10 μm and 1 mm. The samples were analyzed using the

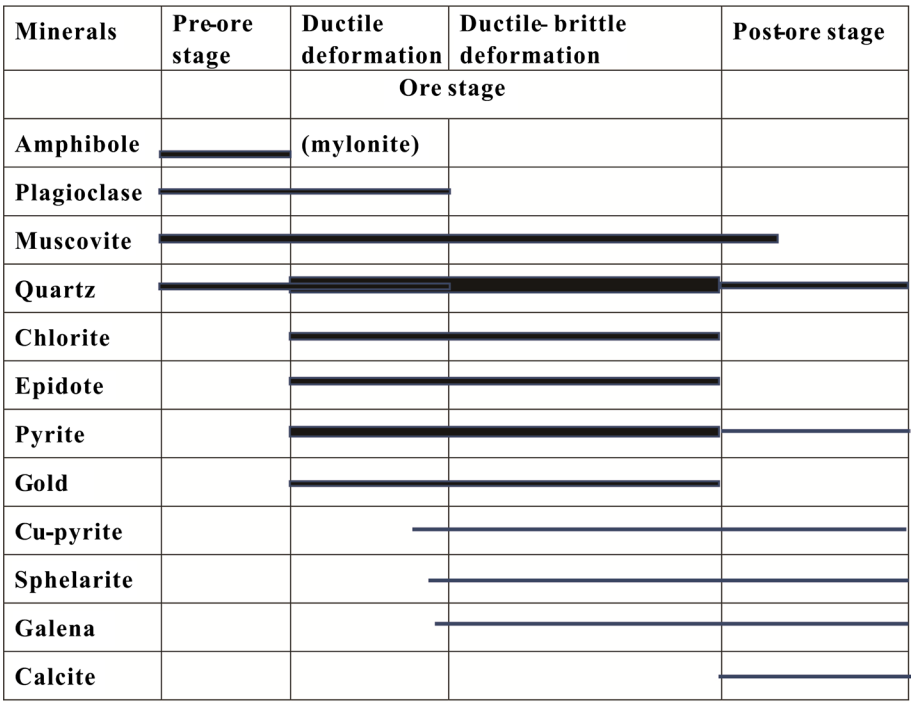

Fig. 3 Paragenetic classification of silicate and ore minerals in the Huangshan orogenic-type gold deposit

ESCALAB 250Xi X-ray photoelectron spectrometer 'Thermo' with monochromated Al-Ka X-ray source (hm: 1486.6 eV, work voltage: 15 kV, power: 150 W and the beam spot size: 500 lm) and were carried out at Zhejiang University, P. R. China.

EPR spectroscopy

The separated quartz and pyrite samples were crushed using steel mortar and agate mortar to decrease the grain size to 200 μm. The samples have been washed in water for removing the surface impurity and kept in furnace for complete dry. The other mineral inclusions are removed by handpicking under the stereoscopic microscope.

The EPR spectra of pure quartz powder samples were recorded in JEOL TES 100 EPR spectrometer operating at X-band frequency at the Department of Chemistry, Zhejiang University, P. R. China. The EPR spectra are obtained at the following parameters: temperatures of low temperature, room temperature and annealing (500, 800 K), frequency of ~9.4–9.6 GHz, power of ~1.0 mW, scan range of 335 ± 10 mT for low and room temperature and 250 ± 250 mT for annealing.

Laser Raman spectrometer and cooling–heating stage

Six quartz wafer sections were prepared through various stages of cutting, grinding and polishing in both sides of the sample to obtain wafer (200–300 μm) thickness. Doubly polished thin wafers of quartz samples were carefully studied under a polarized light microscope for detailed fluid inclusion petrography. Each wafer was broken into 4–6 mm in sizes. Inclusions from each field of view isolated and grouped were selected for microthermometry (Roedder 1984; Shepherd et al. 1985; Bodnar 1992; Bakker 2003). For microthermometric experiments, Linkam THMSG-600 stage fitted on Olympus BX-51P microscope was used. The unit operates in the temperature range of −186 to +600 °C. The unit is periodically calibrated by synthetic fluid inclusions of CO_2 (triple point −56.6 °C) and pure H_2O (triple point 0.001 °C). The accuracy of the measurement is ±0.2 °C during cooling and ±1 °C during heating. The selected inclusions were analyzed using ('Thermo') XR-dispersive Raman spectrometer with 532 nm, 'Ar' laser and the magnification of 100× in the School of Earth Sciences, Zhejiang University, P. R. China. Data generated on only those inclusions, which have not been decrypted and reproducible during experiment, were used for data interpretation.

Results

Classification of pyrite

Two varieties of pyrite have been recognized: recrystallized pyrite (py1) and euhedral pyrite (py2). Texturally recrystallized pyrite is further classified into three types: sheared pyrite (py1a) through intermediate stage of recrystallized fracture filled (py1b) and recrystallized no fracture

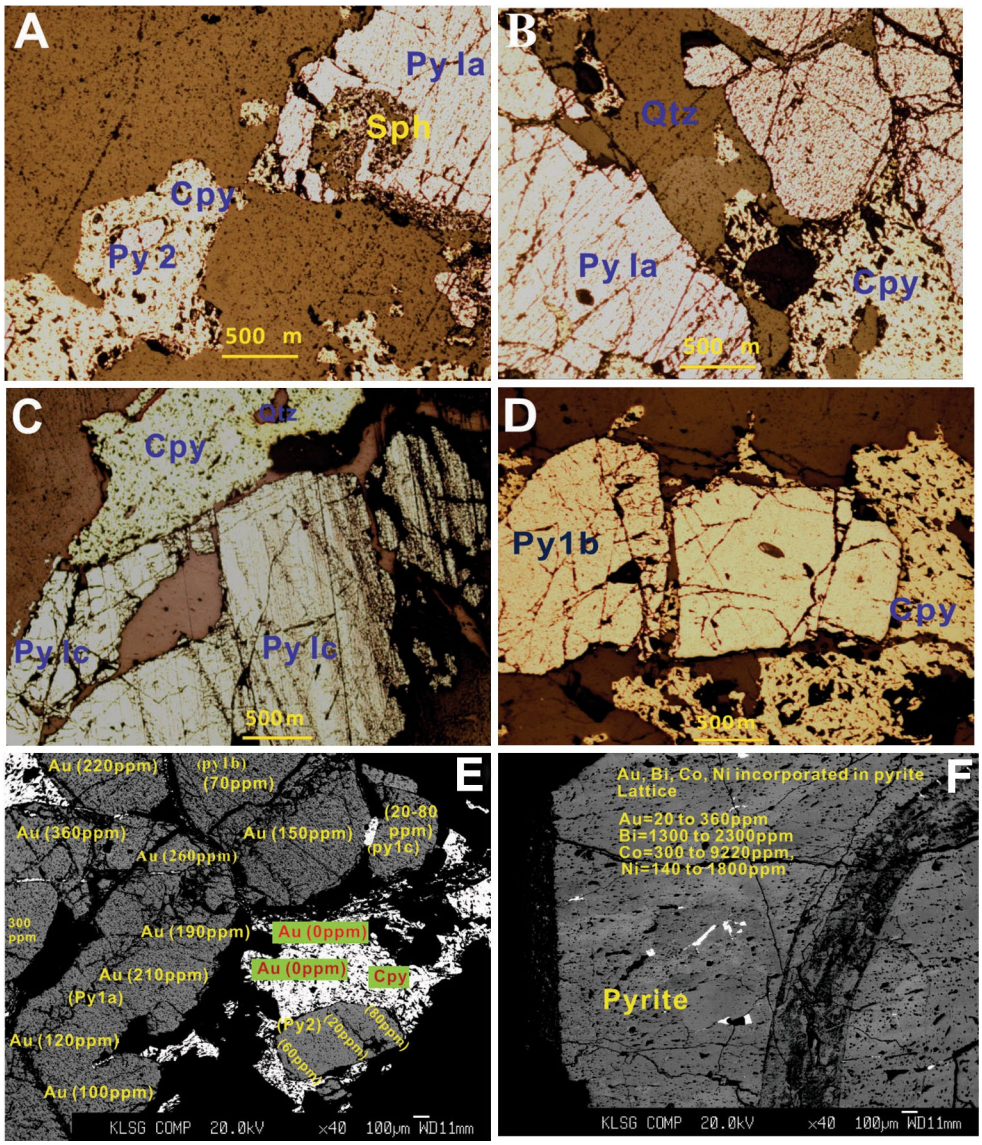

Fig. 4 Reflected light photomicrographs and backscattered images for typical morphology and ore texture in the Huangshan gold deposit. **A**–**D** Different forms of recrystallized pyrite (py1a–py1b–py1c), euhedral pyrite (py2) and pyrite appear as fracturing and intense shearing (ductile zone); and **E**, **F** backscattered electron images and measured concentrations of Au, Co, Ni, Bi. Abbreviations: Py, pyrite; Qtz, quartz; Cpy, chalcopyrite; and Sph, sphalerite

fills (py1c) (Fig. 4). The genetic and textural relationships among py1a, py1b and py1c occurrences have different levels of replaced minerals (gangue and sulfide phases). The py2 occurred as a euhedral crystal and is embedded within chalcopyrite. Pyrite crystals of different forms were possibly formed due to recrystallization from the host metamorphic rock during subsequent metamorphic processes. Well-developed pyrite crystals are controlled by temperature of crystallization, differential stress activity and sulfur fugacity during the subsequent events (Deditius et al. 2014). It is interesting to consider that py2 may be the end product of gold deposition, and there is no gold found in other sulfides. The trace element abundance of recrystallized pyrite and euhedral pyrite is listed in Table 1.

Recrystallized pyrite (py1)

The amount of Co, Ni and Au concentration of recrystallized pyrite varies in py1a, py1b and py1c. The py1a has Co, Ni and Au contents and Co/Ni ratios ranging 9220–7850 ppm, 360–140 ppm, 200–360 ppm and 25–56, respectively, whereas the py1b has Co, Ni, Au and Co/Ni ratios of 5590–5020 ppm, 540–320 ppm, 70–180 ppm and 10–15, respectively. However, the py1c shows Co and Au

Table 1 EPMA results for average trace element abundances in pyrite (py1 and py2) and chalcopyrite in the Huangshan orogenic-type gold deposit

Pyrite	Fe (%)	S (%)	Cu (%)	As (ppm)	Au (ppm)	Co (ppm)	Ni (ppm)	Co/Ni	Bi (ppm)	Tl (ppm)
Py1a	46.30	53.1		0	360	9220	360	25.6	2270	2170
	46.30	53.5		0	260	9210	180	51.1	2390	2080
	46.33	53.8		0	210	7850	140	56.0	2270	2170
	46.29	53.0		0	190	7800	150	52.0	1450	1250
	46.31	53.1		0	100	7600	170	45.0	1450	1370
Py1b	46.13	53.3		0	220	5590	540	10.3	2350	1840
	46.7	53.0		0	150	5210	580	8.9	2170	1600
	46.1	53.1		0	70	5020	320	15.6	2290	1840
Py1c	47.0	52.9		0	80	1260	770	1.6	2260	1910
	46.8	53.0		0	20	1510	860	1.8	2290	1980
Py2	47.3	53.5		0.001	60	1430	1600	0.89	2260	2070
	47.3	53.5		0.006	20	1260	1800	0.7	2250	2040
	47.6	53.2		0.008	80	1320	1650	0.8	2210	2010
Cu–Py	30.9	36.5	34.1	0	0	420	0		1320	1120
	30.7	36.2	34.0	0	0	310	0		2400	1760

contents decrease from 1510 to 1260 ppm and from 80 to 20 ppm, respectively, with increase of Ni abundant from 770 to 860 ppm.

Euhedral pyrite (py2)

The py2 is texturally similar to py1c (different level of trace element enrichment). It shows very low abundances of Co and Au with high Ni abundances. It has Co, Ni, Au and Co/Ni ratios ranging 1430–1260 ppm, 1600–1800 ppm, 20–80 ppm and <1, respectively. The abundance of Au has a decreasing order within a zonal pyrite. The Co and Au concentration decreases with increasing concentration of Ni, reflecting a feature of the trace element variation of Ni > Co in the py2.

XPS results

The X-ray photoelectron spectroscopy was used to characterize the size and chemical state of trace elements, particularly for Au. The concentration of Au in pyrite varies from 360 to 20 ppm. The gold precipitation on pyrite surface is induced by changes in P, T, Eh and pH of ore fluid complexes (Cook and Chryssoulis 1990; Bowers 1991). The interpretation of Au is mainly based on the electrochemistry of $4f_{7/2}$ spectra.

The binding energies of Au $4f_{7/2}$ as determined by XPS from 84.1 to 90.0 eV correspond to chemically bonded gold (Au^0) in quartz and 90–93 eV for Au^{3+} in pyrite. The value of binding energy of Au $4f_{7/2}$ depends on the size and chemical state (Scaini et al. 1997). The binding energy decreases with decreasing size of gold grains, suggesting that valence states of Au^{3+} replaced $2Fe^{2+}$ in the pyrite structure and Au^0 replaced Si in the quartz structure (Fig. 5a–d). Other trace elements in pyrite such as Bi and Co are also detected on pyrite (Fig. 5e, f), implying significant amount of impurities sitting in the pyrite lattice.

EPR results

EPR results of auriferous quartz

The quartz contains numerous atoms of various substitutional and interstitial impurities and paramagnetic centers in the crystal structure. The room temperature EPR spectra of quartz are inactive. The low temperature (107 K) and annealing (500 and 800 K) samples yielded strong resonance lines as identified with the help of '*g*' (gyro-magnetic ratio) values. The '*g*' value is calculated by $E = h\upsilon = g\beta B_o$. While '*g*' is the spectroscopic splitting factor, β is the Bohr magneton and B_o is the external magnetic field (Ikeya 1993). For paramagnetic species in mineral samples, their orbital momentum is quenched due to the crystal field parameters, which reflects symmetry of the environment corresponding to '*g*' value. However, the '*g*' value in mineralized samples is quite different from non-mineralized samples (Matyash et al. 1982; Van Moort and Russell 1987; Van Moort and Brathwaite 1988; Ikeya 1993; Russell and Van Moort 1999).

Al center ($g = 2.027$) and E_1 center ($g = 2.0026$) are detected at a low temperature (107 K) (Fig. 6a) in the study samples. Annealing of quartz samples yielded interstitial impurities of Fe^{3+} and $[GeO_4/Li^+]^0$ or Mn^{2+} ($g = 2.001$). The typical centers are related to a gold-mineralized environment (Russell 1995; Pwa and Van Moort 1999). In non-mineralized samples, these centers are typically absent

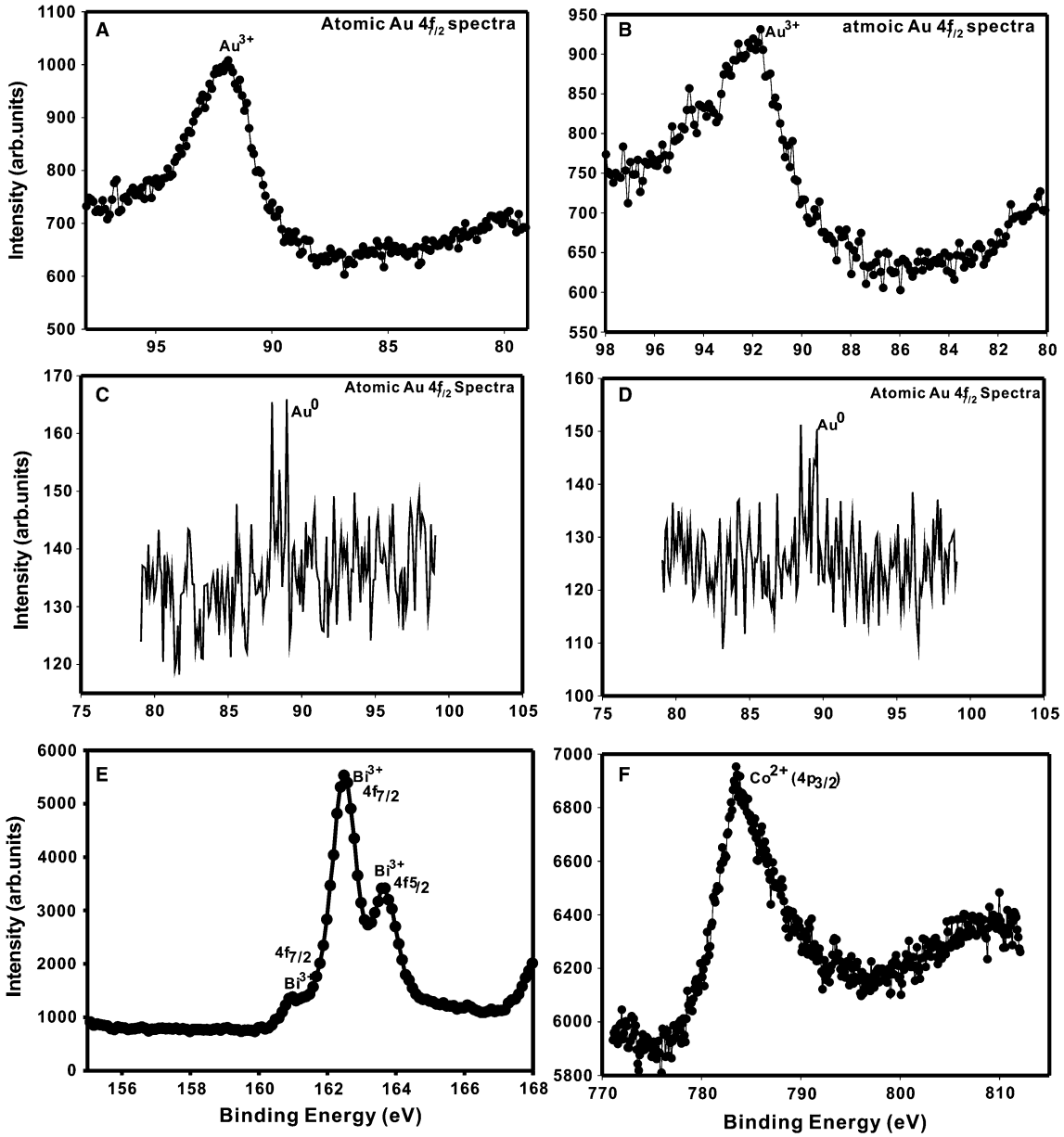

Fig. 5 X-ray photoelectron chemical spectra for the Huangshan orogenic-type gold deposit. **A**, **B** Gold-rich pyrite (Au^{3+}), **C**, **D** auriferous quartz (Au^{0}) and **E**, **F** Bi and Co rich in pyrite

or relatively very low (McQueen et al. 2001). This study highlights the significant understanding of trace element contents, impurities and paramagnetic centers being incorporated into the auriferous quartz lattice. Trace element geochemistry of auriferous quartz and associated impurities compared with other Paleozoic gold deposit are listed in Tables 2 and 3.

EPR results of gold-rich pyrite

EPR results of pyrite samples show Fe^{3+} and Mn^{2+} with a characteristic peak shift observed from room temperature to low temperature and annealing temperature. The EPR spectra clearly indicate the presence of Mn^{2+}, and its '*g*' value ranges from 1.999 to 2.001. The Mn^{2+} is a d^5 ion, and it is very sensitive to distortions from octahedral to tetrahedral symmetry, and the total spins of Mn^{2+} are $\pm 5/2$, $\pm 3/2$ and $\pm 1/2$ (sextets). The six hyperfine splits are called as Kramer's doublets, and the hyperfine coupling constant is obtained from the EPR spectra of Mn^{2+}, which correspond to characteristic peak shift and ionicity (Ikeya 1993; Seshamaheswaramma et al. 2011) (Fig. 6b). The peak shift and ionicity are distinct features observed in gold-mineralized environment.

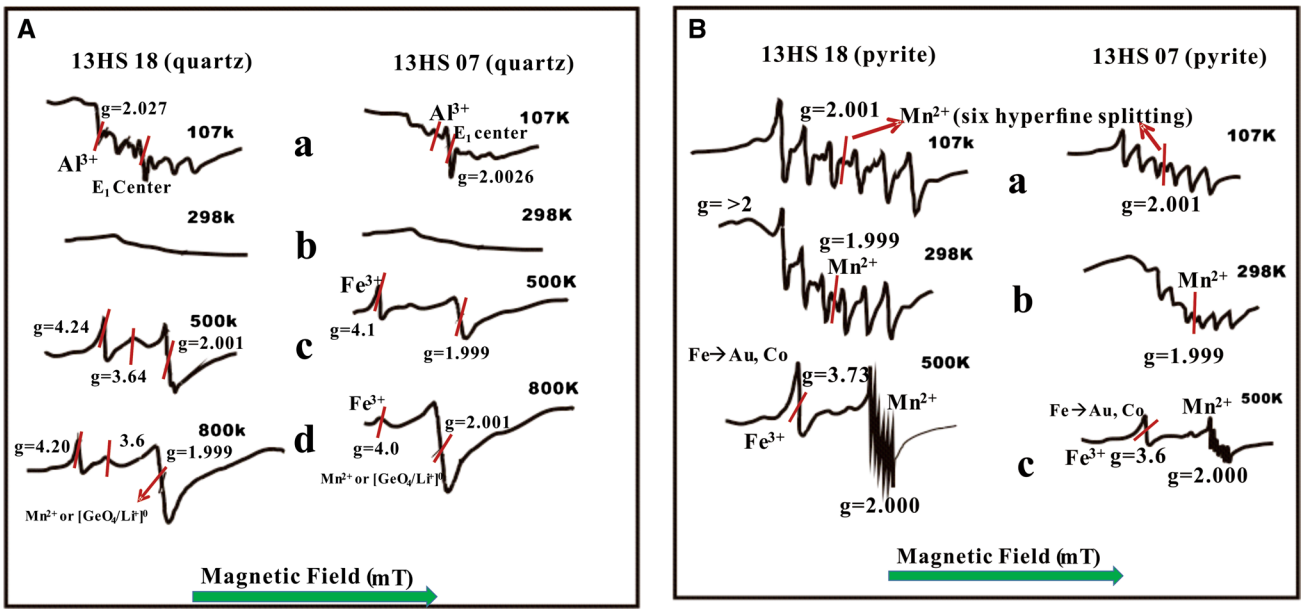

Fig. 6 **A** EPR spectra for auriferous quartz samples from the Huangshan gold deposit. Note: low temperature (107 K), room temperature (298 K) and annealing (500 K, 800 K); and **B** EPR spectra for gold-rich pyrite samples from the Huangshan deposit; low temperature (107 K), room temperature (298 K) and annealing (500 K); and scan range: 335 ± 10 mT in *a*, *b*; 250 ± 250 mT (500 K) in *c*, *d*

Table 2 Trace element abundances (ppm) in auriferous quartz and pyrite samples in Huangshan orogenic-type deposit

Samples	Ge	Li	Co	Ni	Rb	Sr	Ba	V	Cr	Cs
13HS04 (quartz)	5.2	5.3	25.4	3.71	2.4	54.2	11.8	4.6	10.6	<1
13HS05 (quartz)	4.6	7.2	25.7	10.5	6.6	45.5	98.3	26.9	12.1	<1
13HS07 (quartz)	5.9	4.7	14.2	8.3	8.1	112.0	140.0	41.3	6.1	<1
13HS18 (quartz)	4.7	9.5	16.3	2.7	3.7	34.9	40.9	14.9	1.1	<1
13HS04 (pyrite)	<1	<1	954	189	<1	9.8	<1	1.8	5.0	<1
13HS05 (pyrite)	<1	<1	928	210	<1	7.9	<1	1.7	4.8	<1
13HS07 (pyrite)	<1	<1	982	170	<1	12.9	1.5	1.9	5.8	<1
13HS18 (pyrite)	<1	<1	114	91.9	<1	10.1	1.3	1.6	8.0	<1

Table 3 Typical paramagnetic impurities and centers in auriferous quartz (Huangshan) compared with other Paleozoic gold deposits

Gold deposit	Time	Facies/Lithology	Paramagnetism	References
Cowarra deposit	Early Paleozoic	Lower greenschist–facies	Al, Mn, E_1 center, oxygen hole center	McQueen et al. (2001)
Beaconsfield	Early Paleozoic	Sedimentary facies	Al, Ge, Li, Mn, Fe	Russell and Van Moort (1999)
Huangshan	Early Paleozoic	Upper–mid greenschist–facies	Al, Ge, Li, Mn, Fe, Co, Ni, E_1-center	This study

Fluid inclusion study

Fluid inclusion petrography

Fluid inclusions are samples of ore fluid, which yield valuable information about *P–T–X* during mineralization. The genetic classifications of fluid inclusion are done according to the following rules. Isolated fluid inclusions and clusters are interpreted to be primary phases in origin. The inclusions aligned as trails or planar arrays are considered to be secondary phases in origin (Roedder 1984; Bodnar 1985; Wilkinson 2001).

In the auriferous quartz samples, three types of primary fluid inclusions are identified. Type I, type II and type III are aqueous biphase liquid rich ($L_{H_2O} > V_{H_2O}$), carbonic monophase (L_{CO_2} or V_{CO_2}), and aqueous-carbonic

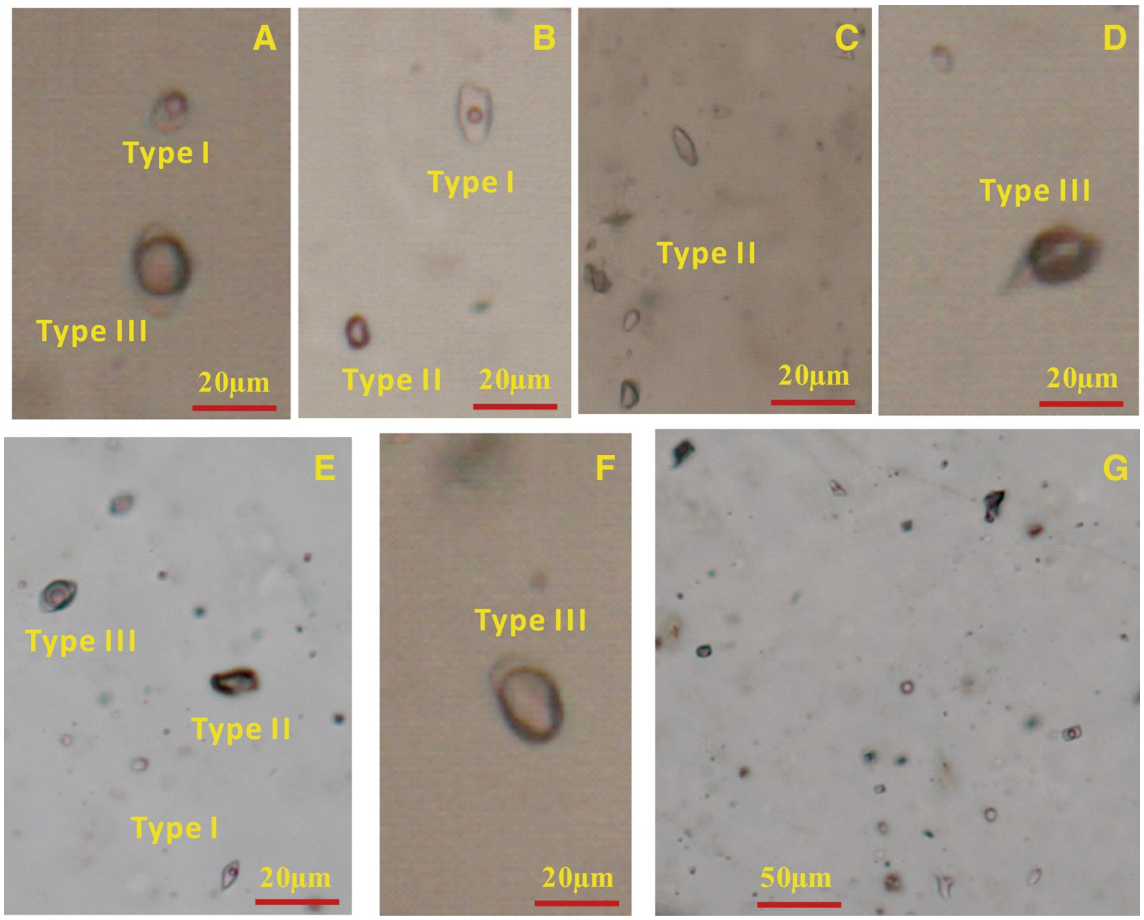

Fig. 7 Types of fluid inclusion in auriferous quartz. **A**–**F** For the type I ($L_{H_2O} + V_{H_2O}$), type II (L_{CO_2}) and type III ($L_{H_2O} + L_{CO_2}$), and **G** inclusions observed near crystal growth zone

Table 4 Petrography and microthermometry results of auriferous quartz from Huangshan gold deposit

Type	phase	Size (um)	Shape	T_{mCO_2} (°C)	Tm_{clath} (°C)	T_{hCO_2} (°C)	Tmeut (°C)	Tmice (°C)	Salinity (wt%. NaCl eq)	Th_{tot} (°C)
I	$L_{H_2O} + V_{H_2O}$	2 to 10	Oval Round Triangular Irregular				−18.7 to −12	−4.5 to −0.3	7.2 to 0.5	160 to 295 (L)
II	V_{CO_2}	4 to 12								
III	$L_{H_2O} + L_{CO_2} + V_{H_2O}$	8 to 16		−59.4 to −57.9	6.5 to 8.5	15 to 28 (V)			7 to 3	175 to 328 (V)

T_{mCO_2}, melting temperature of CO_2; Tm_{clath}, temperature of clathrate melting; T_{hCO_2}, homogenization temperature for CO_2; *Tmeut*, eutectic melting temperature; *Tmice*, temperature of ice melting; *Thtot*, total homogenization temperature

inclusion ($L_{H_2O} + L_{CO_2}$) respectively. The size of the inclusion varies from 2 to 16 μm in diameter (Fig. 7). The isolated and group of primary inclusions are chosen for microthermometry and Raman microscopy (Table 4); and coeval and co-existing inclusions of type I and type III are used for *P*–*T* estimation.

Microthermometry

In the type I inclusions, first melting temperatures between −18.7 and −12 °C (NaCl eutectic at −21.2 °C) are observed. The final ice-melting temperature of these inclusions varies from −4.5 to −0.3 °C (cluster between

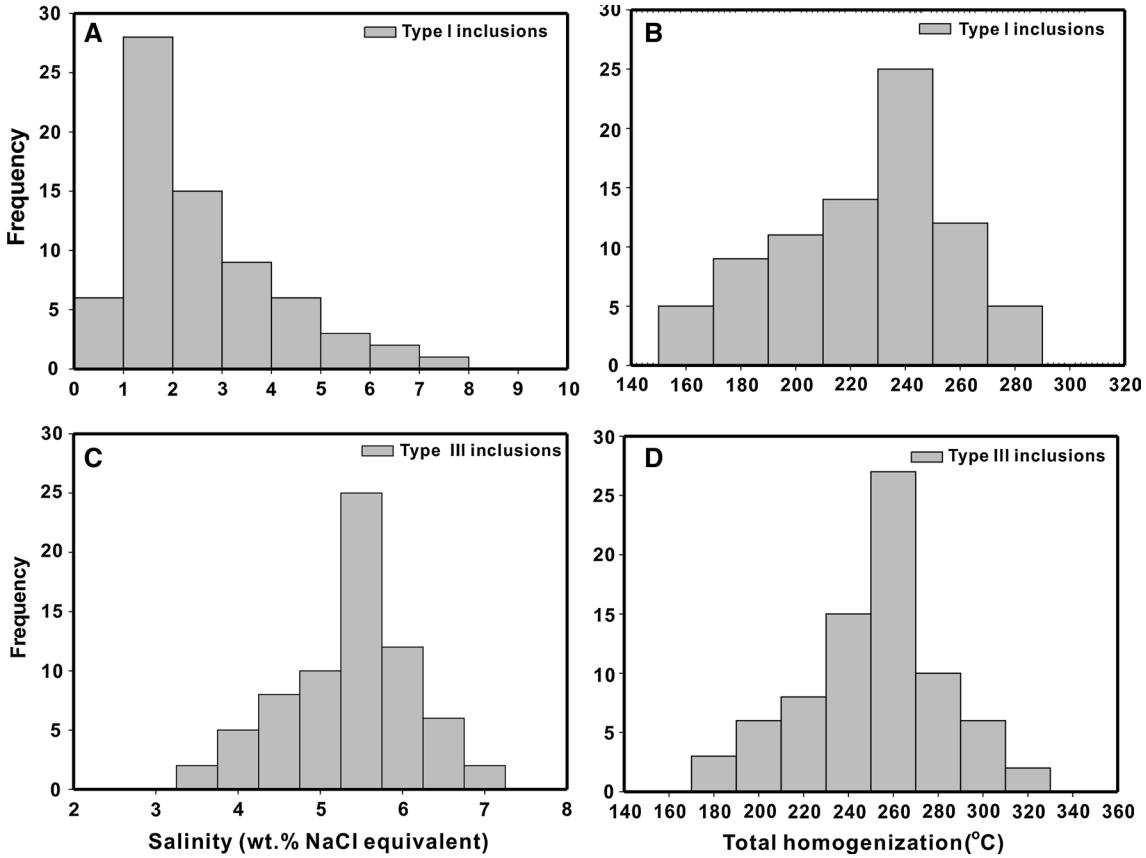

Fig. 8 Histogram plots for auriferous quartz of the Huangshan orogenic-type gold deposit. **A** Temperature of ice melting versus frequency plot for type I inclusions, **B** homogenization temperature versus frequency plot for type I inclusions, **C** salinity versus frequency plot for type III inclusions, and **D** total homogenization temperature versus frequency plot for type III inclusions

−0.3 and −1.5 °C) corresponding to salinity values of 7.2–0.5 wt% NaC1 equivalent, according to Goldstein and Reynolds (1994) classification. The type I inclusions are homogenized into liquid ($L_{H_2O} + V_{H_2O} \rightarrow L_{H_2O}$) between 160 and 295 °C. For type III inclusions, T_{mCO_2} was recorded to lie between −59.4 and −57.9 °C (presence of low amount of volatile phases). Final clathrate-melting temperature was observed at 6.5–8.5 °C (7–3 wt% NaCl equivalent) (cluster between 8.1 and 8.5 °C). The partial homogenization temperature of type III inclusions varies from 15 to 28 °C ($L_{H_2O} + L_{CO_2} + V_{CO_2} \rightarrow L_{H_2O} + V_{CO_2}$). The total homogenization temperature of type III inclusion ranges from 175 to 328 °C ($L_{H_2O} + V_{CO_2} \rightarrow V_{CO_2}$). The histograms of type I and type III inclusions are plotted in Fig. 8.

Raman microscopy results

Few primary inclusions are selected to determine the composition of molecular species using Raman microscopy. The identification of different phases is obtained based on the position of Raman shift in the spectra (Burke 2001; Burruss 2003). The type I to type III inclusions show the presence of H_2O and CO_2 phases with typical Raman shift values, such as 1284 and 1387 cm^{-1} for CO_2 doublets in the type II and III inclusions and 3300–3400 cm^{-1} for H_2O in type I inclusions (Fig. 9).

P–T estimation (isochoric intersection)

The pressure–temperature conditions of gold precipitation have been calculated by intersection of coexisting fluids (type I and type III inclusions) in auriferous quartz. The *P–T* values for isochore were obtained by FLINCOR program (Brown 1989). The homogenization, ice-melting and clathrate-melting temperatures were used for calculation. The equations (Bowers and Helgeson 1983; Zhang and Franz 1987) were used for *P–T* estimation. The *P–T* values of $I_1 = 253$ °C/1250 bar and $I_2 = 218$ °C/780 bar at the point of intersection during entrapment of these fluids are obtained (Fig. 10).

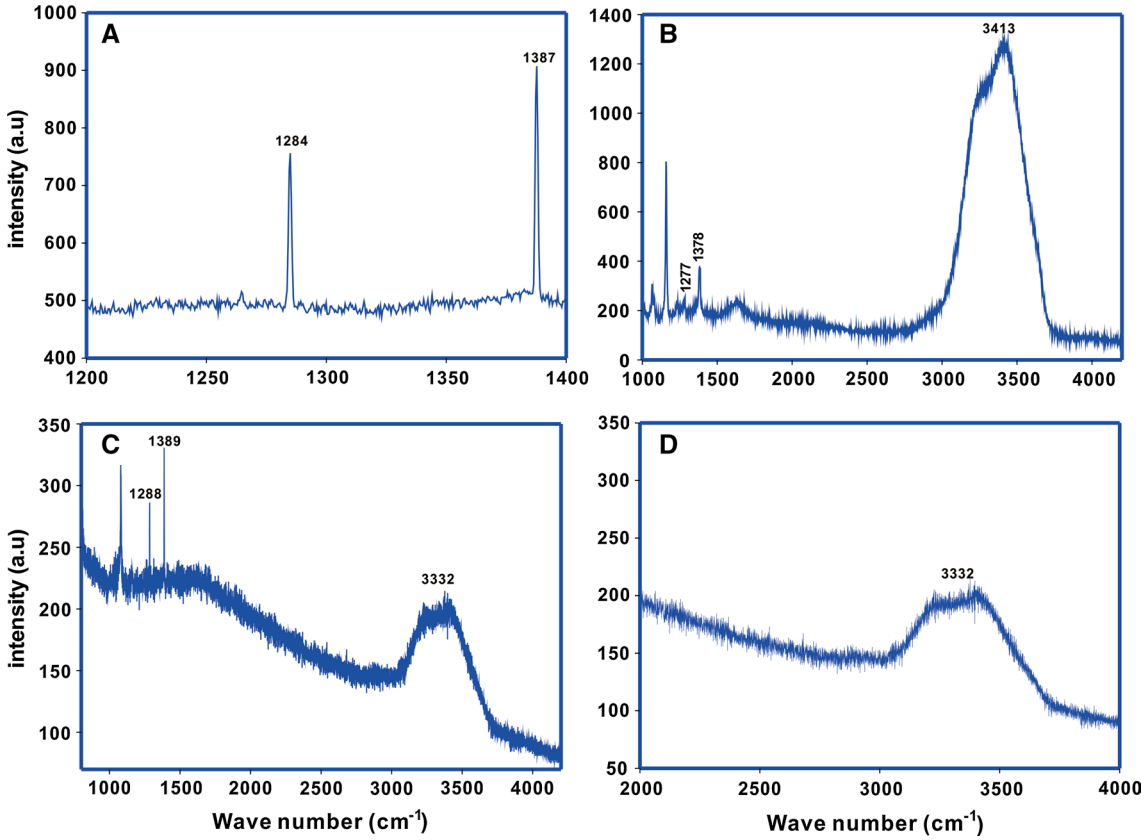

Fig. 9 Laser Raman spectra of fluid inclusions in the auriferous quartz in the Huangshan deposit, **A** CO_2 doublets (1284 and 1387 cm^{-1}) in type II inclusion, **B** CO_2 doublets (1277 and 1378 cm^{-1}) and H_2O liquid rich (3413 cm^{-1}) in type III inclusion, **C** CO_2 doublets (1288 and 1389 cm^{-1}) and H_2O liquid poor (3332 cm^{-1}) in type III inclusion and **D** H_2O vapor (3320 cm^{-1}) in type III inclusion

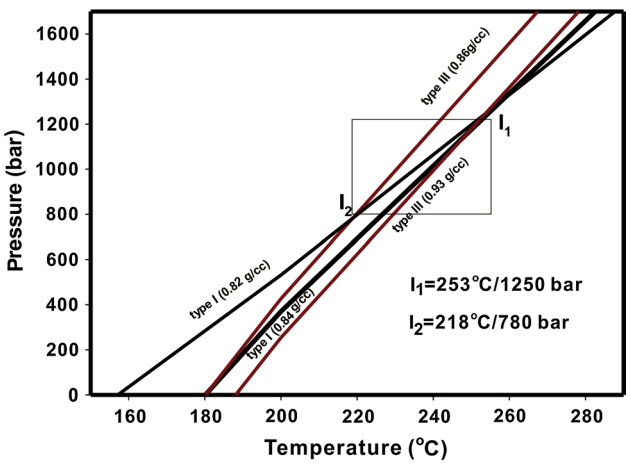

Fig. 10 Isochore plot for auriferous quartz vein in ductile shear zone. The *P*–*T* values of $I_1 = 253$ °C/1250 bars and $I_2 = 218$ °C/780 bars at the point of intersection during entrapment of these fluids in Huangshan orogenic-type gold deposit

Discussion

Gold precipitation mechanism

In the Huangshan orogenic-type gold deposit, quartz and pyrite are the main host minerals for invisible Au distribution and other impurities. The Au content in py1a and py1b is relatively higher than those in py1c and py2. Different stages of pyrite show more or less different trace element concentrations. Even a single pyrite crystal contains different levels of trace element incorporation.

Co and Ni are a significant element pair for gold-associated pyrite and important elements for understanding the origin and precipitation of Au in pyrite. However, the EPMA study reveals that Co and Ni are incorporated into pyrite lattice and provide the information about Au-precipitating fluid mechanism, and the processes are controlled by their primary composition via fluid–rock interaction. The

concentrations of Co, Ni and Co/Ni ratios are common in many gold-mineralized environments (Large et al. 2009; Zhao et al. 2011; Deditius et al. 2014). The content of Au increases with increasing concentration of Co and depletion of Ni content. The Huangshan orogenic-type gold deposit is spatially associated with upper–mid greenschist–facies and contains relatively moderate concentration of Ni (140–1800 ppm) and high concentration of Co (360–9220 ppm) in pyrite. Significant differences in the Co and Ni concentrations in pyrite reflect local fluctuations in the bulk fluid chemistry, which may well have been caused by interaction with wall rocks. The ratio of Co/Ni is highly variable in different environments (Bralia et al. 1979; Cook 1996; Cook and Chryssoulis (1990); Large et al. 2009; Cook et al. 2009). The high concentrations of Co (>500 ppm) and Co/Ni > 1 imply pyrite precipitated from high to moderate temperature and hydrothermal origin as pointed by Bralia et al. (1979). The py2 typically contains higher Ni than Co, py2 usually coexists with chalcopyrite, and Co is incorporated in the chalcopyrite lattice in very low amounts, which might indicate that *P–T* changes of crystallization lead to increased Ni from the host rock and the concentration of Ni is relatively absent in chalcopyrite.

The concentration of Au in py1 decreases through py2, and no gold was found in other sulfides. The concentration of gold was incorporated into the pyrite, and interstices with other elements such as Co–Ni interact with $AuHS_2^-$-rich fluids in different stages of pyrite. Therefore, this process, mainly controlled by temperature of crystallization, f_{S2} (sulfur fugacity), and the sulfidation reaction between Au-bearing fluids and the wall rock (Cook and Chryssoulis 1990; Cook et al. 2009), is argued in this study.

Implication for gold-associated impurities

Ge and Li in quartz, and Co and Ni in pyrite are the two important element pairs, and their relative concentration is presumably related to gold mineralization. However, Ge developed the same bonding behavior in quartz, and it can be easily substituted for Si^{4+} in quartz lattice because of its similar ionic size. Li is also a powerful element to determine gold-mineralized environment. However, Pwa and Van Moort (1999) reported no gold if there are no Li and Ge in auriferous quartz. The optimum correlation between gold and the total amount of Ge + Li is >10 ppm. Similarly, Co and Ni developed in pyrite structure. The level of trace elements incorporation and impurities in quartz and pyrite is primarily controlled by ionic potential and types of bonding (Gotze et al. 2001; Larsen et al. 2004; Gotze 2009).

In the Huangshan orogenic-type gold deposit, the precipitation of quartz and pyrite in hydrothermal stage is highly variable. Interstitial elements are accommodated in the vacant spaces produced by lattice defects during shearing events, where there may be charge balance anomalies in the structure of these minerals and the elements are easily remobilized during alteration in quartz (silicification) and pyrite (pyritization) because of relative weakness of the bonding. The amount of trace elements in quartz and pyrite depends on lattice elasticity and rate of crystal growth, which is primarily controlled by metamorphism, shearing events and temperature of crystallization. The concentration of Ge and Li in auriferous quartz is an important compensator ion $[GeO_4/Li^+]^0$. An alternative interpretation of the strong enrichment of Li in quartz may be related to the increasing content of Al in quartz (Ikeya 1993). In summary, the trace element incorporation in quartz and pyrite is mostly controlled by metamorphic-rich fluids during shearing events; the element pairs of Ge–Li–Al in quartz and Mn–Co–Ni in pyrite are the characteristic impurity centers identified in gold-mineralized zone, in which these features are relatively absent in non-mineralized zone.

The behavior of Au in quartz–pyrite vein is mainly controlled by temperature of crystallization, rate of crystal growth, incorporation of Ge–Al–Li and Co–Ni–Mn elements that are interacting with $AuHS_2^-$ complex in the mineralizing fluids under high sulfur fugacity conditions (Becker et al. 2001; Mikhlin et al. 2011; Large et al. 2009; Sung et al. 2009; Thomas et al. 2011; Zhao et al. 2011; Deditius et al. 2014). The precipitation mechanism of Au in pyrite is chemically related to Co–Ni-rich fluids in different generation of pyrite in Huangshan orogenic-type Au deposit.

Ore-forming fluid process

The type I and III inclusions in quartz have the similar range of homogenization temperature of 160–295 °C ($L + V \rightarrow L$) and 175–328 °C ($L_1 + L_2 + V \rightarrow V$), respectively, with different salinities for type I inclusions (7.2–0.5 wt% NaCl equivalent) (cluster between the ice melting at 0.3–1.5 °C (<3 wt% NaCl equivalent) and type III inclusions (7–3 wt% NaCl equivalent) (cluster between the clathrate-melting temperature at 8.1–8.5 °C (<4 wt% NaCl equivalent). The ore mechanism for Huangshan orogenic-type gold deposit accounts for dissolution, transportation and precipitation of ore changes the fluid salinity from higher to lower thermal gradient.

Petrographic evidence reveals that coexisting type I and type III inclusions and different modes of homogenization to liquid and vapor are the effective evidences of immiscible fluid process (Fig. 11). The immiscible fluid process might have been generated by a process of mixing of two independently derived fluids (as aqueous biphase and

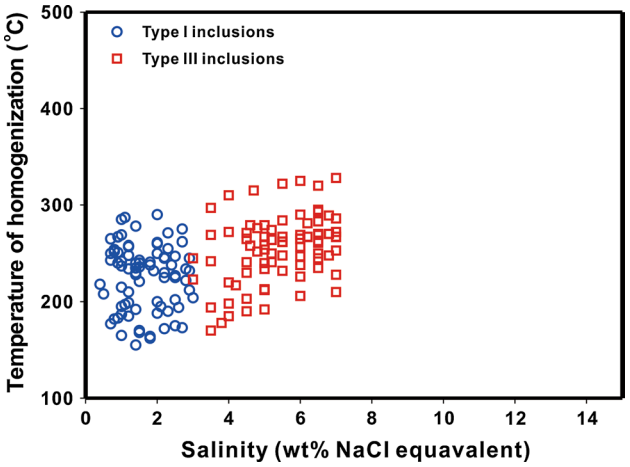

Fig. 11 Salinity versus total homogenization temperature illustrating the distribution pattern of the data points from the Huangshan orogenic-type gold deposit

carbonic fluids); and phase separation and fluid entrapment occurred during Au precipitation. Globally, the boiling fluid process and fluid mixing process have been proposed for many orogenic-type gold deposits (Goldfarb et al. 2001, 2005; Zhou et al. 2015). These fluid processes most likely occur only in shallow environments. Moreover, exsolution of CO_2-rich fluids, occurred mostly in deep-seated environments (ductile zone), is an evidence of immiscible fluid process in the Huangshan deposit unlike fluid mixing or boiling process.

Isochore intersection plot for coexisting fluids (aqueous carbonic and aqueous biphase) reveals *P–T* regimes of fluid entrapment in the zone of ductile event (gold precipitation and hydrothermal alteration). Furthermore, the *P–T* domains of the aqueous biphase (type I) and aqueous-carbonic inclusions (type III) are obtained, and an entailing phase separation from H_2O–CO_2–NaCl fluid responds to pressure decrease, possibly from a middle to upper crustal fluids during advection of the initial metamorphic aqueous-carbonic fluids by expanding the H_2O–NaCl–CO_2 solvus. Although the *P–T* values, obtained by isochore intersection (1250–780 bar and 253–218 °C), are well within the *P–T* window, this observation is common for many orogenic-type gold-mineralizing systems (Goldfarb et al. 2001, 2005; Groves et al. 2003), particularly for upper–medium grade greenschist-hosted deposits being indications of reasonable pressure fluctuation (470 bar), especially for shear zone-related systems. Pressure fluctuation process could have been facilitated by phase separation of an initial H_2O–NaCl–CO_2–$Au(HS)_2$ fluid leading to gold precipitation as previously reported by Wilkinson and Johnston (1996) and Mikucki (1998). Furthermore, the circulating metamorphic fluids are preferentially channeled through pathways determined by ductile shear zones and are perhaps the most important channel ways, in terms of zone of gold precipitation in the Huangshan orogenic-type Au deposit.

Genesis of the Huangshan gold deposit

The Huangshan orogenic-type gold mineralization primarily occurred along Jiangshan–Shaoxing tectonic belt during the early Paleozoic (Chen and Xu 1996; Li et al. 2010b; Zhao et al. 2013; Yao et al. 2014; Ni et al. 2015). The Jiangshan–Shaoxing tectonic belt is an important belt formed during the Neoproterozoic between the Yangtze and Cathaysia blocks. Several Neoproterozoic groups of felsic and mafic intrusive rocks are reported on the Chencai Group along this belt (Ye et al. 1994; Li et al. 2009; Yao et al. 2014). Recent isotopic studies suggested that there was no evidence of the Neoproterozoic metamorphic rocks along this belt (Li et al. 2009; Zhang et al. 2014; Ni et al. 2015). Moreover, the early Paleozoic gold mineralization in the NE Jiang-Shao tectonic belt is consistent with metamorphism of the rocks. These metamorphic rocks developed in Cathaysia inliers during a compressional to extensional environment of continental margin and developed a series of ductile shear zones along this tectonic belt during the early Paleozoic. These ductile shear zones are associated with numerous gold deposits in the NE Jiangshan–Shaoxing belt, such as the Huangshan, Pingshui, Mali, Shiqi, Tongshulin and Zhongao deposits (Zhu et al. 2009; Ni et al. 2015).

The gold mineralization in the Huangshan deposit can be a product of an early Paleozoic orogenic-type gold belt based on the following evidences. (1) The Huangshan gold deposit is spatially associated with a ductile shear zone along the NE Jiangshan–Shaoxing tectonic belt; (2) carbonic fluids are the dominant phases, and the fluid salinity is <7.5 wt% NaCl equivalent. The fluid process suggests evidence of immiscibility, which implies the deposit occurs in deep-seated environments; (3) the common alteration features of sericitization, silicification and pyritization are readily observed (alterations are common phenomena for many orogenic gold deposits); and (4) the Au occurs as an invisible form in different stages of As-free pyrite, which is essentially controlled by Co–Ni and $AuHS_2^-$-rich hydrothermal fluids.

The ore bodies in the Huangshan gold deposit formed in a upper to mid greenschist-facies metamorphism. The deposit is located along the ductile–brittle and ductile shear zone structures, fluids flow through these shear systems (Mattioli et al. 2014; Kisters et al. 1999), with mineralization styles dominated by auriferous quartz–pyrite veins. Orogenic ore-forming hydrothermal systems are dominated by low-saline and CO_2-rich fluids. All of these features suggest that the Huangshan deposit is an orogenic-type gold deposit in South China.

Conclusion

Through the above study of ore mineralogy, trace elements, impurities and fluid inclusion in the Huangshan gold deposit, some important conclusions are made as follows.

1. The Huangshan gold deposit was restricted to the ductile shear zone with a high–medium grade metamorphism that occurred along the Jiangshan–Shaoxing tectonic belt in the Cathaysia inliers during the early Paleozoic.
2. The concentration of gold is mainly controlled by Co–Ni and $AuHS_2^-$-rich hydrothermal fluids in different stages of pyrite.
3. The element pairs of (Ge–Li–Al) in quartz and (Mn–Co–Ni) in pyrite are the characteristic impurity centers identified in gold-mineralized zone.
4. Fluid inclusion study showed relatively low entrapment temperature and carbon dioxide-rich fluids. The coexisting type I and type III inclusions and the same range of homogenization temperature with different mode of homogenization are evidences of immiscible fluid process.
5. The Huangshan orogenic-type gold deposit may be associated with the Wuyi-Yunkai orogeny during the early Paleozoic, including an upper–mid greenschist-facies metamorphism (450–420 Ma).
6. The Huangshan deposit can be explained by a orogenic-type gold deposit, consistent with the age of the early Paleozoic orogeny in South China.

Acknowledgments The authors sincerely thank Y.-H. Hu and S.-Q. Yu of Zhejiang Institute of Geological Survey, H.-L. Chen, C. Rao, L.-F. Meng and X.-Q. Yang of Zhejiang University for their assistance in field and indoor work, J.-H. Zhu and G.-L. Xu for EPMA analyses in Key Laboratory of Submarine Geosciences, State Oceanic Administration of P. R. China, and Joseph Nathaniel Bass (USA) for improving the English level of the manuscript. This study was financially supported by the National Natural Science Foundation of China (No. 41541018), China Geology Survey (Nos. 12120114020801, 2014-04-018-010), Department of Science and Technology of Zhejiang Province (No. 2014C33023), and Department of Land and Resources of Zhejiang Province (Nos. 2015006, 2010001) and Zhejiang Provincial Geological Prospecting Bureau of china (No. 2015005).

References

Bakker RJ (2003) Package FLUIDS 1. Computer programs for analysis of fluid inclusion data and for modeling for bulk fluid properties. Chem Geol 194:3–23

Becker U, Rosso KM, Hochella MFH Jr (2001) The proximity effect on semiconducting mineral surfaces: a new aspect of mineral surface reactivity and surface complexation theory? Geochim Cosmochim Acta 65(16):2641–2649

Bodnar R (1985) Fluid inclusion systematics in epithermal systems. Rev Econ Geol 2:73–97

Bodnar RJ (1992) Can we recognize magmatic fluid inclusions in fossil system based on room temperature phase relations and microthermometric behavior? Geol Surv Rep 279:26–30

Bowers TS (1991) The deposition of gold and other metals: pressure-induced fluid immiscibility and associated stable isotope signatures. Geochim Cosmochim Acta 55:2417–2434

Bowers T, Helgeson HC (1983) Calculation of the thermodynamic and geochemical consequences of non-ideal mixing in the system H_2O–CO_2–NaCl on phase relations in geological systems: metamorphic equilibria at high pressures and temperatures. Am Mineral 68:1059–1075

Bralia A, Sabatini G, Troja F (1979) A revaluation of the Co/Ni ratio in pyrite as geochemical tool in ore genesis problems. Miner Depos 14(3):353–374

Brown PE (1989) FLINCOR: a microcomputer program for the reduction and investigation of fluid-inclusion data. Am Mineral 74:1390–1393

Burke EAJ (2001) Raman microthermometry of fluid Inclusions. Lithos 55:139–158

Burruss RC (2003) Raman spectroscopy of fluid inclusions analysis and Interpretation. Mineral Assoc Can Short Courses 32:279–289

Chen YJ (2006) Orogenic-type deposits and their metallogenic model and exploration potential. Geol China 33:1181–1196 **(in Chinese with English abstract)**

Chen YJ (2010) On epizonogenism and genetic classification of hydrothermal deposits. Earth Sci Front 17:27–34 **(in Chinese with English abstract)**

Chen JF, Jahn BM (1997) Crustal evolution of southeastern China. Nd and Sr isotopic evidence. Tectonophysics 284:101–133

Chen H, Xu B (1996) Isotope tracing and prospecting assessment of gold–silver deposits in Zhejiang Province. Acta Geol Sin 71(3):293–304 **(in Chinese with English abstract)**

Chen YJ, Pirajno F, Wu G, Qi JP, Xiong XL (2012) Epithermal deposits in north Xinjiang, NW China. Int J Earth Sci 101:889–917

Ciobanu CL, Cook NJ, Utsunomiya S, Kogagwa M, Green L, Gilbert S, Wade B (2012) Gold–telluride nano-particles revealed in arsenic-free pyrite. Am Mineral 97:1515–1518

Cook NJ (1996) Mineralogy of the sulphide deposits at Sulitjelma, northern Norway. Ore Geol Rev 11(5):303–338

Cook NJ, Chryssoulis SL (1990) Concentrations of invisible gold in the common sulfides. Can Mineral 28(1):1–16

Cook NJ, Ciobanu CL, Mao J (2009) Textural control on gold distribution in As-free pyrite from the Dongping, Huangtuliang and Hougou gold deposits, North China Craton (Hebei Province, China). Chem Geol 264:101–121

Deditius AP, Reich M, Kesler SE, Utsunomiya S, Chryssoulis SL, Walshe J, Ewing RC (2014) The coupled geochemistry of Au and As in pyrite from hydrothermal ore deposits. Geochim Cosmochim Acta 140:644–670

Fowler WB, Sambasiva Rao P, Weil JA, Wilson TM (1987) P substituted for Si in alpha-quartz: defect structure and properties. Bull Am Phys Soc 32:870

Goldfarb R, Groves D, Gardoll S (2001) Orogenic gold and geologic time: a global synthesis. Ore Geol Rev 18:1–75

Goldfarb RJ, Baker T, Dube B, Groves DI, Hart CJR, Robert F, Gosselin P (2005) Distribution, character, and genesis of gold deposits in metamorphic terrenes. Econ Geol 100th anniversary:407-450

Goldstein RH, Reynolds TJ (1994) Systematics of fluid inclusions in diagenetic minerals: SEPM short course. Soc Sediment Geol 31:199

Gotze J (2009) Chemistry, textures and physical properties of quartz-geological interpretation and technical application. Mineral Mag 73:645–671

Gotze J, Plotze M, Habermann D (2001) Origin, spectral characteristics and practical applications of the cathodoluminescence (CL) of quartz–a review. Mineral Petrol 71:225–250

Groves DI, Goldfarb RJ, Gebre-Mariam M, Hagemann S, Robert F (1998) Orogenic gold deposits: A proposed classification in the context of their crustal distribution and relationship to other gold deposit types. Ore Geol Rev 13(1):7–27

Groves DI, Goldfarb RJ, Robert F, Hart CJ (2003) Gold deposits in metamorphic belts: Overview of current understanding, outstanding problems, future research, and exploration significance. Econ Geol 98(1):1–29

Helmy H, Zoheir B (2015) Metal and fluid sources in a potential world-class gold deposit: El-Sid mine, Egypt. Int J Earth Sci 104:645–661

Ikeya M (1993) New applications of electron spin resonance: dating, dosimetry and microscopy. World Scientific, Singapore

Kerrich R, Goldfarb R, Groves D, Garwin S, Jia Y (2000) The characteristics, origins, and geodynamic settings of supergiant gold metallogenic provinces. Sci China Ser D Earth Sci 43:1–68

Kisters AFM, Meyer FM, Seravkin IB, Znamensky SE, Kosarev AM, Ertl RGW (1999) The geological setting of lode-gold deposits in the central southern Urals: a review. Geol Rundsch 87:603–616

Large RR, Danyushevsky L, Hollit C, Maslennikov V, Meffre S, Gilbert S, Bull S, Scott R, Emsbo P, Thomas H (2009) Gold and trace element zonation in pyrite using a laser imaging technique: implications for the timing of gold in orogenic and Carlin-style sediment-hosted deposits. Econ Geol 104:635–668

Larsen RB, Henderson I, Ihlen PM, Jacamon F (2004) Distribution and petrogenetic behavior of trace elements in granitic pegmatite quartz from South Norway. Contrib Miner Petrol 147:615–628

Li XH, Li WX, Li ZX (2007) On the genetic classification and tectonic implication of the early Yanshanian granitoids in the Nanling Range, South China. Chin Sci Bull 52:1873–1885

Li XH, Li WX, Li ZX, Lo CH, Wang J, Ye MF, Yang YH (2009) Amalgamation between the Yangtze and Cathaysia Blocks in South China: constraints from SHRIMP U–Pb zircon ages, geochemistry and Nd–Hf isotopes of the Shuangxiwu volcanic rocks. Precambr Res 174:117–128

Li XF, Wang CZ, Hua RM, Wei XL (2010a) Fluid origin and structural enhancement during mineralization of the Jinshan orogenic gold deposit, South China. Miner Depos 45:583–597

Li ZX, Li XH, Wartho JA, Clark C, Li WX, Zhang CL, Bao C (2010b) Magmatic and metamorphic events during the early Paleozoic Wuyi–Yunkai orogeny, southeastern South China: New age constraints and pressure-temperature conditions. Geol Soc Am Bull 122:772–793

Mattioli M, Menichetti M, Renzulli A, Toscani L, Salvioli-Mariani E, Suarez P, Murroni A (2014) Genesis of the hydrothermal gold deposits in the Canan area, Lepaguare District, Honduras. Int J Earth Sci 103:901–928

Matyash I, Bagmut N, Litovchenko A, Proshko VY (1982) Electron paramagnetic resonance study of new paramagnetic centers in microcline-perthites from pegmatites. Phys Chem Miner 8:149–152

McQueen K, Pwa A, Van Moort J (2001) Geochemical and electron paramagnetic characteristics of quartz from a multi-stage vein environment, Cowarra gold deposit, New South Wales. J Geochem Explor 72:211–221

Mikhlin YL, Romanchenko AS (2007) Gold deposition on pyrite and the common sulfide minerals: an STM/STS and SR-XPS study of surface reactions and Au nano particles. Geochim Cosmochim Acta 71:5985–6001

Mikhlin Y et al (2011) Understanding the initial stages of precious metals precipitation: Nanoscale metallic and sulfidic species of gold and silver on pyrite surfaces. Ore Geol Rev 42(1):47-54

Mikucki EJ (1998) Hydrothermal transport and depositional processes in Archean lode-gold systems: a review. Ore Geol Rev 13:307–321

Ni P, Wang GG, Chen H, Xu YF, Guan SJ, Pan JY, Li L (2015) An Early Paleozoic orogenic gold belt along the Jiang-Shao Fault, South China: evidence from fluid inclusions and Rb–Sr dating of quartz in the Huangshan and Pingshui deposits. J Asian Earth Sci 103:87–102

Nuttall R, Weil J (1981a) The magnetic properties of the oxygen-hole aluminum centers in crystalline SiO_2.I.$[AlO_4]^0$. Can J Phys 59:1696–1708

Nuttall R, Weil J (1981b) The magnetic properties of the oxygen-hole aluminum centers in crystalline SiO_2.II.$[AlO_4/H^+]^+$ and $[AlO_4/Li^+]^+$. Can J Phys 59:1709–1718

Nuttall R, Weil J (1981c) The magnetic properties of the oxygen-hole aluminum centers in crystalline SiO_2.III.$[AlO_4]^+$. Can J Phys 59:1886–1892

Palenik CS, Utsunomiya S, Reich M, Kesler SE, Wang L, Ewing RC (2004) "Invisible" gold revealed: direct imaging of gold nano particles in a Carlin-type deposit. Am Mineral 89:1359–1366

Pirajno F, Bagas L (2002) Gold and silver metallogeny of the South China Fold Belt: a consequence of multiple mineralizing events? Ore Geol Rev 20:109–126

Pirajno F, Bagas L, Hickman AH (1997) Gold mineralization of the Chencai-Suichang uplift and tectonic evolution of Zhejiang Province, Southeast China. Ore Geol Rev 12:35–55

Pirajno F, Ernst RE, Borisenko AS, Fedoseev G, Naumov EA (2009) Intraplate magmatism in Central Asia and China and associated metallogeny. Ore Geol Rev 35(2):114–136

Pwa A, Van Moort J (1999) Electron paramagnetic resonance (EPR) spectroscopy in massive sulphide exploration, Rosebery mine area, western Tasmania, Australia. J Geochem Explor 65:155–172

Reich M, Kesler SE, Utsunomiya S, Palenik CS, Chryssoulis SL, Ewing RC (2005) Solubility of gold in arsenian pyrite. Geochim Cosmochim Acta 69:2781–2796

Reich M, Utsunomiya S, Kesler SE, Wan L, Ewing RC, Becker U (2006) Thermal behavior of metal nanoparticles in geologic materials. Geology 34:1033–1036

Ren JS (1990) On the geotectonics of Southeastern China. Acta Geol Sin 64(2):275–288

Roedder E (1984) Fluid inclusions. In: Ribbe PH (ed) Mineralogical Society of America. Rev Mineral 12:644–648

Russell DW (1995) The characterization of quartz and gold in the Beaconsfield and Lefroy areas, northern Tasmania. Unpublished PhD Thesis, p 335

Russell D, Van Moort J (1999) The chemical characterization of auriferous vein quartz, Beaconsfield gold mine, Tasmania. J Geochem Explor 67:191–200

Scaini MJ, Bancroft GM, Knipe SW (1997) An XPS, AES and SEM study of the interactions of gold and silver chloride species with PbS and FeS_2: comparison to natural samples. Geochim Cosmochim Acta 61:1223–1231

Seshamaheswaramma K, Reddy GU, Reddy AV, Lakshmi Reddy S, Frost R, Endo T (2011) EPR and optical absorption spectral studies on sphalerite mineral. Spectrochim Acta Part A Mol Biomol Spectrosc 81:308–331

Shepherd TJ, Rankin AH, Alderton D (1985) A practical guide to fluid inclusion studies. Blackie, Glasgow

Su W, Zhang H, Hu R, Ge X, Xia B, Chen Y, Zhu C (2012) Mineralogy and geochemistry of gold-bearing arsenian pyrite from the Shuiyindong Carlin-type gold deposit, Guizhou, China: implications for gold depositional processes. Miner Depos 47:653–662

Sung YH, Brugger J, Ciobanu CL, Pring A, Skinner W, Nugus M (2009) Invisible gold in arsenian pyrite and arsenopyrite from a multistage Achaean gold deposit: sunrise Dam,

Eastern Goldfields Province, Western Australia. Miner Depos 44:765–791

Thomas HV, Large RR, Bull SW, Maslennikov V, Berry RF, Fraser R, Froud S, Moye R (2011) Pyrite and pyrrhotite textures and composition in sediments, laminated quartz veins, and reefs at Bendigo gold mine, Australia: insights for ore genesis. Econ Geol 106:1–31

Van Moort J, Brathwaite R (1988) Electron paramagnetic resonance (EPR) powder spectra of epithermal quartz from the Martha Hill gold–silver deposit, Waihi, New Zealand. Bicentennial Gold. Geol Soc Aust Ext Abstr 23:575–578

Van Moort J, Russell D (1987) Electron spin resonance of auriferous and barren quartz at Beaconsfield, Northern Tasmania. J Geochem Explor 27:227–237

Weil JA (1984) A review of electron spin spectroscopy and its application to the study of paramagnetic defects in crystalline quartz. Phys Chem Miner 10:149–165

Weil JA (1993) A review of the EPR spectroscopy of the point defects in α-quartz: the decade, 1982–1992, The Physics and Chemistry of SiO_2 and the Si-SiO_2 Interface 2. Springer, pp 131–144

Wilkinson J (2001) Fluid inclusions in hydrothermal ore deposits. Lithos 55:229–272

Wilkinson J, Johnston J (1996) Pressure fluctuations, phase separation, and gold precipitation during seismic fracture propagation. Geology 24:395–398

Wilson T, Weil J, Rao P (1986) Electronic structure of the interstitial lithium-associated electron trap in crystalline quartz. Phys Rev B 34:6053

Yao J, Shu L, Santosh M, Xu Z (2014) Palaeozoic metamorphism of the Neoproterozoic basement in NE Cathaysia: zircon U–Pb ages, Hf isotope and whole-rock geochemistry from the Chencai Group. J Geol Soc 173:2013–2036

Ye Y, Lan YQ, Chen YS (1994) ^{40}Ar–^{39}Ar chronology and metamorphic age of Chencai Group, Zhejiang Province, China. Acta Petrol Sin 10:193–201 **(in Chinese with English abstract)**

Zhang Y, Franz JD (1987) Determination of homogenization temperature and densities of supercritical fluids in the system NaC1–KC1–$CaC1_2$–H_2O using synthetic fluid inclusions. Chem Geol 64:335–350

Zhang LC, Xiao WJ, Qin KZ, Ji JS, Yang XK (2004) Types, geological features and geodynamic significances of gold–copper deposits in the Kanggurtag metallogenic belt, eastern Tianshan, NW China. Int J Earth Sci 93:224–240

Zhang CL, Santosh M, Zhu QB, Chen XY, Huang WC (2014) The Gondwana connection of South China: evidence from monazite and zircon geochronology in the Cathaysia Block. Gondwana Res 26(2):627–653

Zhao HX, Frimmel HE, Jiang SY, Dai BZ (2011) LA-ICP-MS trace element analysis of pyrite from the Xiaoqinling gold district, China: implications for ore genesis. Ore Geol Rev 43(1):142–153

Zhao C, Ni P, Wang GG, Ding JY, Chen H, Zhao KD, Cai YT, Xu YF (2013) Geology, fluid inclusion, and isotope constraints on ore genesis of the Neoproterozoic Jinshan orogenic gold deposit, South China. Geofluids 13:506–527

Zhong ZQ, You ZD, Zhou HW, Han YJ (1996) The evolution and basic structural framework of the basement of the Yunkai uplift. Reg Geol China 56:36–43 **(in Chinese with English abstract)**

Zhou ZJ, Chen YJ, Jiang SY, Hu CJ, Qin Y, Zhao HX (2015) Isotope and fluid inclusion geochemistry and genesis of the Qiangma gold deposit, Xiaoqinling gold field, Qinling Orogen, China. Ore Geol Rev 66:47–64

Zhu AQ, Zhang YS, Lu ZD, Zhang CL (2009) The study minerogenetic series and metallogenic districts of the metallic and nonmetallic ore deposits in Zhejiang Province. Geological Publishing House, Beijing, China, p 433 **(in Chinese with English abstract)**